

# Two-Stage Attitude Control for Direct Imaging of Exoplanets with a CubeSat Telescope

Connor Beierle<sup>a</sup>, Andrew Norton<sup>b</sup>, Bruce Macintosh<sup>b</sup>, and Simone D’Amico<sup>a</sup>

<sup>a</sup>Space Rendezvous Laboratory, Stanford University, Stanford, CA

<sup>b</sup>Kavli Institute for Particle Astrophysics and Cosmology, Stanford University, Stanford, CA

## ABSTRACT

This work outlines the design and development of a prototype CubeSat space telescope to directly image exoplanets and/or exozodiacal dust. This prototype represents the optical payload of the miniaturized distributed occulter/telescope (mDOT), a starshade technology demonstration mission combining a 2 meter scale microsatellite occulter and a 6U CubeSat telescope. Science requirements for the mDOT experiment are presented and translated into engineering requirements for the attitude determination and control subsystem (ADCS). The ADCS will utilize a triad of reaction wheels for coarse pointing and a tip tilt mirror for fine image stabilization down to the sub-arcsecond level. A two-stage attitude control architecture is presented to achieve precise pointing necessary for stable acquisition of diffraction limited imagery. A multiplicative extended Kalman filter is utilized to estimate the inertial attitude of the vehicle and provide input into the aforementioned controller. A hardware-in-the-loop optical stimulator is used to stimulate the payload with scenes highly representative of the space environment from a radiometric and geometric stand point. Scenes rendered to the optical stimulator are synthesized in closed-loop based off a high-fidelity numerical simulation of the underlying disturbances, orbital and attitude dynamics. Performance of the two-stage attitude control loop is quantified and demonstrates the ability to achieve sub-arcsecond pointing using a telescope payload prototype.

**Keywords:** exoplanet, exozodiacal dust, CubeSat, attitude determination and control, tip tilt mirror

## 1. INTRODUCTION

Detection and characterization of exoplanets in recent years have predominantly relied on indirect methods, which measure an exoplanet’s effect on the light of their parent star. Most notably, NASA’s Kepler mission is now responsible for more than one thousand confirmed exoplanet discoveries.<sup>1</sup> The indirect methods used for most discoveries to date allow scientists to determine the mass, size, and temperature of a planet, but provide little information about its chemical composition. However, only a few exoplanets have been detected by direct imaging. Direct imaging allows the properties of the planet to be deduced from spectral data and is not subject to the detection constraints of indirect methods. Spectroscopy data collected from direct images would allow scientists to identify key biosignature gases such as oxygen, water, and carbon dioxide.

A promising candidate for direct imaging of exoplanets is a pair of an occulter and a telescope spacecraft, referred to as a distributed occulter/telescope or starshade. Starshades have been the subject of a number of studies including NASA’s New Worlds Observer,<sup>2</sup> but the resulting mission designs are extremely large, requiring extensive intersatellite separations and deployment in deep space. The Space Rendezvous Laboratory (SLAB) at Stanford is investigating the feasibility of a Miniaturized Distributed Occulter Telescope (mDOT) mission to allow deployment of a pair of satellites in Earth orbit, drastically reducing the expected mission costs.<sup>3–6</sup> mDOT would use an occulter at a distance of 500 [km] from a 10 [cm] aperture telescope to improve confidence in the optical and formation flying technologies needed for full-scale starshade missions. mDOT is intended to image exozodiacal dust and Jovian exoplanets at short visible and ultraviolet (UV) wavelengths. Size and distribution of the exozodiacal particles are of scientific interest. Moreover, the distribution can indicate the orientation of the planetary system, as well as hint at hidden exoplanets. mDOT would help satisfy the goal identified in the Decadal Survey of characterizing zodiacal emission around stars.<sup>7</sup>

---

To whom correspondence should be addressed. E-mail: cbeierle@stanford.edu

The potential applications of CubeSats in distributed space science missions is a relatively understudied topic. CubeSats offer a cheap alternative to large monolithic satellite platforms, but due to their small size, they are limited in their utility. However, steadily improving capabilities of CubeSat components, especially in the Guidance, Navigation and Control (GN&C) domain, open new frontiers for CubeSat applications. Placing the telescope on-board of a CubeSat aligns with the objective to reduce the size, complexity and cost of the mission. While the scientific utility will be reduced as compared with large scale missions, mDOT will serve an important role as a technology demonstrator for starshade feasibility, CubeSat formation flying and precision pointing capabilities.

Detection of exozodiacal dust and Jovian exoplanets with a CubeSat sized telescope as proposed in mDOT, will require precise pointing and formation keeping. More broadly, many other science applications could be achieved with a CubeSat and a 10-cm scale telescope. Some of these require high-quality (diffraction-limited) imaging, which is challenging to achieve on CubeSat platforms. Precision pointing in the CubeSat form factor has most recently been studied and launched for the ASTERIA mission.<sup>8</sup> ASTERIA utilizes reaction wheels and a two-axis piezoelectric positioning stage for precise line of sight pointing at the arcsecond-level. However, it has a very short focal length and hence very large pixel scale projected onto the sky. It's pointing requirements are driven by the need to keep a star stably on a particular location within a pixel for photometric stability, but due to the extremely coarse pixels it does not demonstrate diffraction-limited imaging. This study will focus on engineering an attitude control solution which has the ability to achieve both coarse pointing and fine image stabilization at the sub-arcsecond level for sustained periods of time in the presence of environmental and internal disturbances. Such a capability would be applicable to many CubeSat science missions.

The outline of the paper is as follows. Section 2 establishes the design of the mDOT telescope payload prototype analyzed in this study. Section 3 describes the dynamics modeling effort, which utilizes a satellite simulation containing models of attitude/orbital dynamics and relevant perturbations. Section 4 formulates the two-stage attitude control architecture used to achieve precision pointing in the presence of environmental and internal perturbations. This control algorithm will rely on filtered quantities computed in Section 5. Section 6 describes the hardware-in-the-loop (HIL) verification approach utilized to stimulate the telescope payload prototype with an optical stimulator. Section 7 presents results utilizing the numerical simulation and the HIL testbed. Conclusions and ways forward are provided in Section 8.

## 2. TELESCOPE PAYLOAD PROTOTYPE

The telescope spacecraft design presented by Kolmas *et al.*<sup>3</sup> is taken to be 6U CubeSat, with 2U allocated for the telescope payload. The telescope spacecraft is assumed to carry out the observations in eclipse. Pointing stability is critical throughout the 1000 [sec] exposure. If telescope pointing is not kept stable enough, observations of the science target would travel across multiple pixels and degrade signal-to-noise ratio (SNR) of the results. The attitude determination and control system (ADCS) selected in this study was the Blue Canyon Technology XACT unit.<sup>9</sup> The XACT unit features three reaction wheels with pointing accuracies outlined in Table 1.

Specification	Value
$1\sigma$ Pointing Accuracy	$\pm 0.003$ [deg] for 2 axes $\pm 0.007$ [deg] for 3rd axis
LEO Lifetime	3 [years]
Mass	0.85 [kg]
Volume	10 x 10 x 5 [cm]

Table 1. Blue Canyon Technology XACT attitude control unit characteristics<sup>9</sup>

Given a target observation in the visible spectrum, and a payload diameter of 10 [cm], Nyquist-sampled diffraction limited observations require pointing accuracies in the 1-10 [as] range.<sup>5</sup> As seen from Table 1, the XACT unit is unable to achieve this level of pointing accuracy. A tip tilt (TT) mirror is used to achieve a finer level of image stabilization necessary for the aforementioned science objective. The TT mirror is a micro-electrical mechanical systems (MEMS) device (S6180 Mirrorcle Technologies, Inc.) which sits conjugate to the

entrance pupil.<sup>10</sup> The TT mirror provides highly repeatable, fast optical beam steering across two axes, while requiring ultra-low power. Specifications for the S6180 TT mirror are outlined in Table 2.

Specification	Value
Diameter	5 [mm]
Mechanical Range	$\pm 1$ [deg]
Resonant Frequency	1200 [Hz]
Driver Resolution	16 [bit]
Angular Precision	250 [mas]

Table 2. Mirrorcle Technologies S6180 TT mirror technical specifications<sup>10</sup>

Since the TT mirror is 5 [mm] in diameter, incoming light from the 10 [cm] aperture needs to be demagnified to fit on the mirror. A pair of lenses sitting between the entrance pupil and the TT mirror are used to demagnify the incoming light. The incoming light is demagnified to a 4.8 [mm] diameter, which provides a 1 [mm] circular buffer at the perimeter of the mirror. Light reflecting off the mirror then passes through an additional set of lenses which focus the light onto a CMOS detector. While the final optical design for telescope payload would be compact enough for a 2U payload, this prototype payload was designed and built with the goal of demonstrating the functionality and performance of the above controller architecture for precise image stabilization without the constraint of fitting in a 2U volume. With this design relaxation in mind, the plate scale of the CMOS sensor was selected to have pixels subtending 2 [as], as shown in Table 3.

Specification	Value
Focal Length	500 [mm]
Pixel Pitch	5.2 [ $\mu\text{m}$ ]
Format	1280 $\times$ 1024
Plate Scale	2.15 [as/pixel]

Table 3. ThorLabs DCC1545M CMOS camera<sup>11</sup>

### 3. DYNAMICS MODELING AND SIMULATION

In order to assess the feasibility of the attitude determination and control subsystem of the telescope spacecraft, a high-fidelity simulation of the orbital and attitude dynamics was created using the Space Rendezvous Laboratory Satellite Software toolbox, also known as  $\mathcal{S}^3$ . This software library is written in C/C++ to limit computational overhead and enable agile transitions to flight computers. The core C/C++ functionality is also accessible in the MATLAB/Simulink environment through the use of MEX function wrappers and S-functions. An overview of  $\mathcal{S}^3$  is shown in Figure 1.

A detailed discussion of the orbital dynamics simulation capabilities and perturbation models implemented in  $\mathcal{S}^3$  is available in Ref [12]. The remainder of this section will focus on presenting the models of the spacecraft attitude dynamics, environmental and internal disturbances. An overarching analysis of environmental perturbations from aerodynamic drag to solar radiation pressure are considered since the orbit regime of mDOT has not been finalized.

#### 3.1 Attitude Dynamics

The time evolution of a rigid body’s orientation with respect to an inertial reference frame is governed by Euler’s differential equation of rotational motion, as shown by

$$\mathbf{M}^{S/S_{\text{cm}}} = \frac{\mathcal{I}d}{dt} [\mathbf{H}^{S/S_{\text{cm}}}] = \frac{\mathcal{P}d}{dt} [\mathbf{H}^{S/S_{\text{cm}}}] + {}^{\mathcal{I}\rightarrow\mathcal{P}}\boldsymbol{\omega} \times \mathbf{H}^{S/S_{\text{cm}}}, \quad (1)$$

where  $\mathbf{M}^{S/S_{\text{cm}}}$  are moments acting on system  $S$  about the system center of mass ( $S_{\text{cm}}$ ),  $\mathbf{H}^{S/S_{\text{cm}}}$  is the angular momentum of  $S$  taken about  $S_{\text{cm}}$  in the Earth-centered inertial (ECI) reference frame  $\mathcal{I}$ ,  $\mathcal{P}$  is the principal

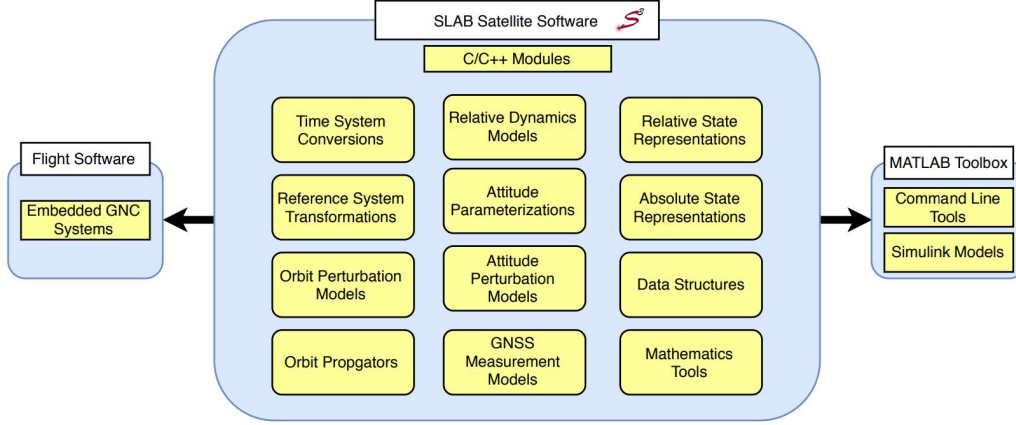


Figure 1. SLAB Satellite Software modules and software structure.<sup>12</sup>

reference frame with origin  $S_{\text{cm}}$  and aligned with the principal axes of  $S$ , and  ${}^{\mathcal{I}\rightarrow\mathcal{P}}\boldsymbol{\omega}$  is the angular velocity of  $\mathcal{P}$  with respect to  $\mathcal{I}$ . Note that the left superscript preceding the derivative operator denotes what frame a derivative is computed in.

For the dual-spin telescope spacecraft,  $\mathbf{H}^{S/S_{\text{cm}}}$  can be decomposed into the angular momentum of the rigid satellite body and the reaction wheels

$$\mathbf{H}^{S/S_{\text{cm}}} = \mathbf{I}_P {}^{\mathcal{I}\rightarrow\mathcal{P}}\boldsymbol{\omega} + \mathbf{I}_R {}^{\mathcal{I}\rightarrow\mathcal{R}}\boldsymbol{\omega}, \quad (2)$$

where  $\mathbf{I}_P$  is the moments of inertia of  $P$  about  $S_{\text{cm}}$ ,  $\mathbf{I}_R$  is the moment of inertia of the reaction wheels about  $S_{\text{cm}}$ ,  ${}^{\mathcal{I}\rightarrow\mathcal{R}}\boldsymbol{\omega}$  is the angular velocity of the reaction wheels with respect to  $\mathcal{I}$ .

Combining Equations 1-2, and solving for the time derivative of  ${}^{\mathcal{I}\rightarrow\mathcal{P}}\boldsymbol{\omega}$  yields

$$\frac{{}^{\mathcal{P}}d}{{}^{\mathcal{I}}dt} [{}^{\mathcal{I}\rightarrow\mathcal{P}}\boldsymbol{\omega}] = \mathbf{I}_P^{-1} \left( \mathbf{M}^{S/S_{\text{cm}}} - \frac{{}^{\mathcal{P}}d}{{}^{\mathcal{I}}dt} [\mathbf{I}_R {}^{\mathcal{I}\rightarrow\mathcal{R}}\boldsymbol{\omega}] - {}^{\mathcal{I}\rightarrow\mathcal{P}}\boldsymbol{\omega} \times [\mathbf{I}_P {}^{\mathcal{I}\rightarrow\mathcal{P}}\boldsymbol{\omega} + \mathbf{I}_R {}^{\mathcal{I}\rightarrow\mathcal{R}}\boldsymbol{\omega}] \right) \quad (3)$$

This non-linear set of differential equations are numerically integrated (with MATLAB/Simulink ODE8: Dormand-Prince), to compute the time evolution of  ${}^{\mathcal{I}\rightarrow\mathcal{P}}\boldsymbol{\omega}$  used in the ground-truth simulation.

### 3.2 Attitude Kinematics

In order to fully describe the attitude motion, the variations of the attitude parameters must be expressed as a function of  ${}^{\mathcal{I}\rightarrow\mathcal{P}}\boldsymbol{\omega}$ . For this study, the scalar-last quaternion convention,  ${}^{\mathcal{I}\rightarrow\mathcal{P}}\mathbf{q}$  is used to encode the alignment of  $\mathcal{P}$  with respect to  $\mathcal{I}$ , and is defined as

$${}^{\mathcal{I}\rightarrow\mathcal{P}}\mathbf{q} \triangleq [q_1 \quad q_2 \quad q_3 \quad q_4]^T = \begin{bmatrix} \hat{\mathbf{n}} \sin(\alpha/2) \\ \cos(\alpha/2) \end{bmatrix} \quad (4)$$

where  $\hat{\mathbf{n}}$  is the eigenaxis and  $\alpha$  is the angle of rotation about the eigenaxis from  $\mathcal{I}$  to  $\mathcal{P}$ . Note that  $\hat{\mathbf{n}}$  is fixed in  $\mathcal{I}$ . The discrete-time kinematic quaternion equations<sup>13</sup> for a time step,  $\Delta t$ , are

$${}^{\mathcal{I}\rightarrow\mathcal{P}}\mathbf{q}_{t+1} = \boldsymbol{\Omega}({}^{\mathcal{I}\rightarrow\mathcal{P}}\boldsymbol{\omega}_t) {}^{\mathcal{I}\rightarrow\mathcal{P}}\mathbf{q}_t \quad (5)$$

with

$$\Omega \left( \overset{\mathcal{I} \rightarrow \mathcal{P}}{\boldsymbol{\omega}} \right) = \frac{1}{\omega} \begin{bmatrix} \omega c_\omega & \omega_3 s_\omega & -\omega_2 s_\omega & \omega_1 s_\omega \\ -\omega_3 s_\omega & \omega c_\omega & \omega_1 s_\omega & \omega_2 s_\omega \\ \omega_2 s_\omega & -\omega_1 s_\omega & \omega c_\omega & \omega_3 s_\omega \\ -\omega_1 s_\omega & -\omega_2 s_\omega & -\omega_3 s_\omega & \omega c_\omega \end{bmatrix} \approx \mathbf{I}_{4,4} + \frac{1}{2} \begin{bmatrix} 0 & +\omega_3 & -\omega_2 & +\omega_1 \\ -\omega_3 & 0 & +\omega_1 & +\omega_2 \\ +\omega_2 & -\omega_1 & 0 & +\omega_3 \\ -\omega_1 & -\omega_2 & -\omega_3 & 0 \end{bmatrix} \Delta t \quad (6)$$

and

$$c_\omega \triangleq \cos \left( \frac{\omega \Delta t}{2} \right) \quad (7)$$

$$s_\omega \triangleq \sin \left( \frac{\omega \Delta t}{2} \right) \quad (8)$$

where  $\omega$  is the 2-norm of  $\overset{\mathcal{I} \rightarrow \mathcal{P}}{\boldsymbol{\omega}}$ , and  $\omega_i$  (for  $i = 1, 2, 3$ ) are the projections of  $\overset{\mathcal{I} \rightarrow \mathcal{P}}{\boldsymbol{\omega}}$  along the coordinate axes of  $\mathcal{P}$ , as shown by

$$\omega_i \triangleq \overset{\mathcal{I} \rightarrow \mathcal{P}}{\boldsymbol{\omega}} \cdot \hat{\mathbf{p}}_i \quad (9)$$

### 3.3 Environmental and Internal Disturbances

#### 3.3.1 Gravity Gradient

Infinitesimal gravitational forces acting on a body vary as a function of the distance from Earth. The result is a gravity gradient torque,  $\vec{\mathbf{M}}_{\text{gg}}$ , which acts on  $S$ . In the principal frame, this torque evaluates to

$$\mathbf{M}_{\text{gg}} = \frac{3\mu}{\left\| \overset{E_0 \rightarrow S_{\text{cm}}}{\mathbf{r}} \right\|^5} \begin{bmatrix} r_2 r_3 (I_{33} - I_{22}) \\ r_1 r_3 (I_{11} - I_{33}) \\ r_1 r_2 (I_{22} - I_{11}) \end{bmatrix}_{\mathcal{P}} \quad (10)$$

where  $\mu$  is the gravitational constant of Earth,  $I_{ii}$  are the principal moments of inertia of  $S$  taken about  $S_{\text{cm}}$ , and  $r_i$  are the projections of the satellite's position vector relative to Earth,  $\overset{E_0 \rightarrow S_{\text{cm}}}{\mathbf{r}}$ , along the coordinate axes of  $\mathcal{P}$ , as shown below

$$r_i \triangleq \overset{E_0 \rightarrow S_{\text{cm}}}{\mathbf{r}} \cdot \hat{\mathbf{p}}_i \quad (11)$$

#### 3.3.2 Solar Radiation Pressure

Radiation incident on the spacecraft's surface produces a force which, when not acting through the vehicle's center of mass, produces a torque on the vehicle. The force,  $\vec{\mathbf{f}}_i$ , due to solar radiation pressure on an illuminated planar satellite panel is<sup>13</sup>

$$\vec{\mathbf{f}}_i = -\frac{F_s A_i (\hat{\mathbf{n}}_i \cdot \hat{\mathbf{s}})}{c} \left[ (1 - C_s) \hat{\mathbf{s}} + 2 \left( C_s (\hat{\mathbf{n}}_i \cdot \hat{\mathbf{s}}) + \frac{1}{3} C_d \right) \hat{\mathbf{n}} \right] \quad (12)$$

where  $F_s = 1367$  [W/m<sup>2</sup>] is the solar constant,  $c = 3.8 \times 10^8$  [m/s] is the speed of light,  $A_i$  and  $\hat{\mathbf{n}}_i$  are the area and surface normal of panel  $i$ ,  $\hat{\mathbf{s}}$  is the normalized position vector from  $S_{\text{cm}}$  to the Sun,  $S_0$ ,  $C_s$  and  $C_d$  are the specular and diffuse reflectance coefficients.

The torque due to solar radiation pressure is the sum of these forces acting through a lever arm,  $\overset{S_{\text{cm}} \rightarrow \text{CP}_i}{\mathbf{r}}$ , between  $S_{\text{cm}}$  and the center of pressure of panel  $i$ ,  $\text{CP}_i$ .

$$\vec{\mathbf{M}}_{\text{srp}} = \sum \epsilon (\hat{\mathbf{n}}_i \cdot \hat{\mathbf{s}}) \gamma \left( \overset{E_0 \rightarrow S_{\text{cm}}}{\mathbf{r}}, \overset{E_0 \rightarrow S_0}{\mathbf{r}} \right) \left( \overset{S_{\text{cm}} \rightarrow \text{CP}_i}{\mathbf{r}} \times \vec{\mathbf{f}}_i \right) \quad (13)$$

where  $\epsilon$  is an indicator function determining if the angle,  $\theta$ , between the  $i^{\text{th}}$  panel normal and another unit vector is positive, as shown by

$$\epsilon(\theta) \triangleq \begin{cases} 0 & \text{if } \theta \leq 0 \\ 1 & \text{otherwise} \end{cases} \quad (14)$$

and  $\gamma$  is an indicator function determining if the satellite is in sunlight or Earth's shadow, as shown by

$$\gamma(E_{0 \rightarrow S_{\text{cm}}}, E_{0 \rightarrow S_0}) \triangleq \begin{cases} 0 & \text{if } \epsilon\left(\frac{E_{0 \rightarrow S_{\text{cm}}}}{\|\mathbf{r}\|} \cdot \frac{E_{0 \rightarrow S_0}}{\|\mathbf{r}\|}\right) = 0 \text{ and } r_{\perp} < R_e \\ 1 & \text{otherwise} \end{cases} \quad (15)$$

where  $R_e = 6378$  [km] and  $r_{\perp}$  is the component of the satellite's position vector perpendicular to the normalized position vector from Earth to Sun

$$r_{\perp} \triangleq \left\| E_{0 \rightarrow S_{\text{cm}}} - \left( E_{0 \rightarrow S_{\text{cm}}} \cdot \frac{E_{0 \rightarrow S_0}}{\|\mathbf{r}\|} \right) \frac{E_{0 \rightarrow S_0}}{\|\mathbf{r}\|} \right\| \quad (16)$$

### 3.3.3 Aerodynamic Drag

Aerodynamic torque results from the impingement of atmospheric gas molecules on spacecraft surfaces. The aerodynamic force acting on the  $i^{\text{th}}$  panel's center of pressure is

$$\vec{\mathbf{f}}_i = -\frac{1}{2} C_D \rho \|\vec{\mathbf{v}}\|^2 A_i \left( \frac{\vec{\mathbf{v}}}{\|\vec{\mathbf{v}}\|} \cdot \hat{\mathbf{n}}_i \right) \frac{\vec{\mathbf{v}}}{\|\vec{\mathbf{v}}\|} \quad (17)$$

where  $C_D$  is a drag coefficient,  $\rho$  is the local density of the atmosphere,  $A_i$  and  $\hat{\mathbf{n}}_i$  are the area and outward surface normal of the  $i^{\text{th}}$  satellite panel, and  $\vec{\mathbf{v}}$  is the velocity of  $S_{\text{cm}}$  relative to the local atmosphere,  $A_0$ , as shown by

$$\vec{\mathbf{v}} \triangleq \frac{\mathcal{I}d}{dt} [E_{0 \rightarrow S_{\text{cm}}} - E_{0 \rightarrow A_0}] \quad (18)$$

Assuming the atmosphere rotates with the same angular velocity as the Earth,  $\vec{\boldsymbol{\omega}}^{\mathcal{I} \rightarrow \mathcal{E}}$ , this relative velocity can be easily calculated by differentiating  $E_{0 \rightarrow A_0}$  in an Earth-fixed frame,  $\mathcal{E}$ , since  $A_0$  is assumed fixed in  $\mathcal{E}$ .

$$\vec{\mathbf{v}} = \frac{\mathcal{I}d}{dt} [E_{0 \rightarrow S_{\text{cm}}}] - \frac{\mathcal{E}d}{dt} [E_{0 \rightarrow A_0}] - \vec{\boldsymbol{\omega}}^{\mathcal{I} \rightarrow \mathcal{E}} \times E_{0 \rightarrow A_0} \quad (19)$$

$$= \frac{\mathcal{I}d}{dt} [E_{0 \rightarrow S_{\text{cm}}}] - \vec{\boldsymbol{\omega}}^{\mathcal{I} \rightarrow \mathcal{E}} \times E_{0 \rightarrow A_0} \quad (20)$$

$$= \frac{\mathcal{I}d}{dt} [E_{0 \rightarrow S_{\text{cm}}}] - \vec{\boldsymbol{\omega}}^{\mathcal{I} \rightarrow \mathcal{E}} \times E_{0 \rightarrow S_{\text{cm}}} \quad (21)$$

Note that the transition from Equation 20 to 21 utilizes the fact that  $A_0$  and  $S_{\text{cm}}$  are instantaneously coincident, and that  $A_0$  is continuously redefined throughout the simulation.

The aerodynamic torque is the sum of the aerodynamic drag forces acting through each panels' lever arm

$$\vec{\mathbf{M}}_{\text{aero}} = \sum \epsilon \left( \hat{\mathbf{n}}_i \cdot \frac{\vec{\mathbf{v}}}{\|\vec{\mathbf{v}}\|} \right) \left( S_{\text{cm}} \vec{\mathbf{r}}^{\text{CP}_i} \times \vec{\mathbf{f}}_i \right) \quad (22)$$

### 3.3.4 Magnetic Disturbance Torque

The interaction between the Earth's magnetic field,  $\vec{\mathbf{B}}$ , and the satellite's magnetic dipole,  $m_{sc}$ , produces a magnetic disturbance torque acting on the vehicle. This torque is given by

$$\vec{\mathbf{M}}_{\text{mag}} = \vec{\mathbf{m}}_{sc} \times \vec{\mathbf{B}} \quad (23)$$

To a first order approximation, the Earth's magnetic field in  $\mathcal{I}$  can be modeled as

$$\vec{\mathbf{B}} = -B_0 \frac{R_e^3}{\|\vec{\mathbf{r}}_{E_0 \rightarrow S_{cm}}\|^3} \left[ 3 \left( \frac{\vec{\mathbf{m}} \cdot \vec{\mathbf{r}}_{E_0 \rightarrow S_{cm}}}{\|\vec{\mathbf{r}}_{E_0 \rightarrow S_{cm}}\|^3} \right) \frac{\vec{\mathbf{r}}_{E_0 \rightarrow S_{cm}}}{\|\vec{\mathbf{r}}_{E_0 \rightarrow S_{cm}}\|} - \vec{\mathbf{m}} \right] \quad (24)$$

where  $B_0$  is the dipole strength,  $R_e = 6371$  [km] is the radius of the Earth, and  $\vec{\mathbf{m}}$  is the Earth's dipole direction. In reference frame  $\mathcal{I}$ ,  $\vec{\mathbf{m}}$  can be computed with the dipole's co-elevation,  $\theta$ , and the Greenwich mean sidereal time,  $\alpha$ , as shown by

$$\vec{\mathbf{m}} = \begin{bmatrix} \sin \theta \cos \alpha \\ \sin \theta \sin \alpha \\ \cos \theta \end{bmatrix}_{\mathcal{I}} \quad (25)$$

### 3.3.5 Reaction Wheel Disturbances

Reaction wheel imbalances contribute to an internal disturbance torque acting on the vehicle. These reaction wheel disturbances are modeled as a linear superposition of  $n$  sinusoidal modes

$$\vec{\mathbf{M}}_x = \sum_{i=1}^{N_h} M_{x_i} (\Omega(t)) \sin \left( 2\pi h_i \Omega(t) t + \phi_i^{M_{\text{rad}}} \right) \quad (26)$$

$$\vec{\mathbf{M}}_y = \sum_{i=1}^{N_h} M_{y_i} (\Omega(t)) \sin \left( 2\pi h_i \Omega(t) t + \phi_i^{M_{\text{rad}}} + \frac{\pi}{2} \right) \quad (27)$$

$$\vec{\mathbf{M}}_z = \sum_{i=1}^{N_h} M_{z_i} (\Omega(t)) \sin \left( 2\pi h_i \Omega(t) t + \phi_i^{M_{\text{axial}}} \right) \quad (28)$$

where  $\Omega(t)$  is the reaction wheel speed,  $h_i$  are the harmonic coefficients,  $\phi$  is the initial phases of a harmonic and  $M_x, M_y, M_z$  are the harmonic amplitudes about the reaction wheel axes. This model is taken from Shields *et al.*<sup>14</sup>

## 4. CONTROL

The two-stage control architecture presented in this work utilizes reaction wheels for coarse pointing and a tip tilt mirror for fine image stabilization. The control law used by the reaction wheels,  $\mathbf{u}_{rw}$ , is a non-linear proportional derivative (PD) controller composed of a feedback and feed-forward signal

$$\mathbf{u}_{rw} = \underbrace{\mathbf{K}_p \mathbf{e}_{1:3} + \mathbf{K}_d \left( \overset{\mathcal{I} \rightarrow \mathcal{P}}{\boldsymbol{\omega}}_d - \overset{\mathcal{I} \rightarrow \mathcal{P}}{\boldsymbol{\omega}} \right)}_{\text{feedback}} + \underbrace{\overset{\mathcal{I} \rightarrow \mathcal{P}}{\boldsymbol{\omega}} \times \left[ \mathbf{I}_P \overset{\mathcal{I} \rightarrow \mathcal{P}}{\boldsymbol{\omega}} + \mathbf{I}_R \overset{\mathcal{I} \rightarrow \mathcal{R}}{\boldsymbol{\omega}} \right]}_{\text{feed-forward}} \quad (29)$$

where  ${}^{\mathcal{I} \rightarrow \mathcal{P}} \boldsymbol{\omega}_d$  is the desired angular velocity of  $\mathcal{P}$  with respect to  $\mathcal{I}$ , and  $\mathbf{e}_{1:3}$  is the vector part of the error quaternion. The error quaternion encodes the rotation from the current attitude,  ${}^{\mathcal{I} \rightarrow \mathcal{P}} \mathbf{q}$ , to the desired attitude,  ${}^{\mathcal{I} \rightarrow \mathcal{P}} \mathbf{q}_d$ , as shown by

$$\mathbf{e} \triangleq {}^{\mathcal{I} \rightarrow \mathcal{P}} \mathbf{q}_d \otimes \left( {}^{\mathcal{I} \rightarrow \mathcal{P}} \mathbf{q} \right)^{-1} \quad (30)$$

This control input produces an angular acceleration of the reaction wheels, as shown by

$$\mathbf{u}_{\text{rw}} = -\mathbf{I}_R \frac{{}^{\mathcal{P}d}}{dt} \left[ {}^{\mathcal{I} \rightarrow \mathcal{R}} \boldsymbol{\omega} \right] \quad (31)$$

A micro-electrical mechanical systems (MEMS) tip/tilt (TT) mirror (model S6180) from Mirrorcle Technologies is used for fine pointing. The TT mirror has  $\pm 1$  [deg] of mechanical throw, is driven by a 16-bit high-voltage driver and has a resonant frequency of 1 [kHz]. The TT mirror is actuated so that motion of the target being observed is stabilized on a complementary metal oxide semiconductor (CMOS) sensor. This fine stabilization is necessary for long integration detections of dim exoplanets and/or exozodiacal dust.

Once coarse pointing and stabilization of the payload is achieved using reaction wheels, a light emitting diode (LED) on the back of the occulter can be detected. Before engaging the TT control loop, this reference LED will exhibit motion on the CMOS detector due to residual jitter from the coarse pointing loop. By calculating bearing angles to the reference LED in the payload frame, differential corrections can be computed and sent to the TT mirror. These corrections will stabilize both the reference LED and the science target on the CMOS sensor.

Bearing angles to the reference LED,  $d\boldsymbol{\theta}$ , are computed using a pinhole model

$$d\boldsymbol{\theta} = \left[ \frac{u-u_0}{f} \quad \frac{v-v_0}{f} \right]^T \quad (32)$$

where  $u$  and  $v$  are the horizontal and vertical pixel coordinates of the centroid of the reference LED,  $u_0$  and  $v_0$  are the coordinates of the CMOS principal point, and  $f$  is the focal length of the payload in pixels.

The bearing angles computed in Equation 32 serve as a differential update to the TT reference signal

$$\boldsymbol{\theta} = \boldsymbol{\theta}_0 + d\boldsymbol{\theta} \quad (33)$$

where  $\boldsymbol{\theta}_0$  and  $\boldsymbol{\theta}$  are the previous and updated TT angular positions. These angular positions are used with an offline calibration to determine what voltage should be sent to the individual axes of the TT mirror.

Since the TT mirror has finite range and bandwidth, this control loop is only closed when the reaction wheel loop has settled to within 0.1 [deg] of sensed angular error.

#### 4.1 Path Planner

For large pointing errors between the initial vehicle attitude,  ${}^{\mathcal{I} \rightarrow \mathcal{P}} \mathbf{q}$ , and final target attitude,  ${}^{\mathcal{I} \rightarrow \mathcal{P}} \mathbf{q}_t$  an intermediate reference frame is used to guide the controller towards the final orientation. This intermediate frame is taken to be  ${}^{\mathcal{I} \rightarrow \mathcal{P}} \mathbf{q}_d$  in Equation 30

$${}^{\mathcal{I} \rightarrow \mathcal{P}} \mathbf{q}_d \triangleq \begin{bmatrix} \hat{\mathbf{n}} \sin(e_\theta/2) \\ \cos(e_\theta/2) \end{bmatrix} \quad (34)$$

with

$$e_\theta(t) \triangleq E_\theta (1 - e^{-\lambda t}) \quad (35)$$

where  $\lambda$  is the path planner time constant,  $e_\theta$  and  $E_\theta$  are rotation angles about the eigenaxis,  $\hat{\mathbf{n}}$ , to the desired and target reference frames,  ${}^{\mathcal{I} \rightarrow \mathcal{P}} \mathbf{q}_d$  and  ${}^{\mathcal{I} \rightarrow \mathcal{P}} \mathbf{q}_t$ , respectively.

## 5. MULTIPLICATIVE EXTENDED KALMAN FILTER

The filtering approach utilized in this work is a nonlinear variant of the Kalman Filter known as the Multiplicative Extended Kalman Filter (MEKF). The MEKF utilizes a quaternion to estimate the absolute spacecraft attitude and a set of Euler angles to represent the attitude error computed in the measurement update. This architecture avoids violating the quaternion unit norm constraint, and has been discussed extensively in literature.<sup>15,16</sup> The state vector,  $\mathbf{x}$ , in Equation 36 is composed of small angles,  $\alpha$ , which have a zero mean expectation.

$$\mathbf{x} = [\alpha_x \quad \alpha_y \quad \alpha_z]^T \quad (36)$$

### 5.1 Predict

The state vector stays constant during the MEKF predict step, and the absolute attitude,  ${}^{\mathcal{I} \rightarrow \mathcal{P}} \mathbf{q}$ , is propagated kinematically forward in time, as shown by

$$\mathbf{x}_{t+1|t} = \mathbf{x}_{t|t} \quad (37)$$

$${}^{\mathcal{I} \rightarrow \mathcal{P}} \mathbf{q}_{t+1|t} = \Omega \left( {}^{\mathcal{I} \rightarrow \mathcal{P}} \boldsymbol{\omega}_t \right) {}^{\mathcal{I} \rightarrow \mathcal{P}} \mathbf{q}_{t|t} \quad (38)$$

For the predict step using this state vector, the covariance update is

$$\boldsymbol{\Sigma}_{t+1|t} = \mathbf{A} \boldsymbol{\Sigma}_{t|t} \mathbf{A}^T + \mathbf{Q}_t \quad (39)$$

where  $\boldsymbol{\Sigma}_{t+1|t}$  is the state covariance prediction at time  $t+1$  given measurements up to time  $t$ ,  $\mathbf{Q}_t$  is the process noise, and  $\mathbf{A}_t$

$$\mathbf{A}_t = I_{3,3} + \frac{s_\omega}{\omega} \left[ {}^{\mathcal{I} \rightarrow \mathcal{P}} \boldsymbol{\omega}_t \times \right] + \left( \frac{1 - c_\omega}{\omega^2} \right) \left[ {}^{\mathcal{I} \rightarrow \mathcal{P}} \boldsymbol{\omega}_t \times \right] \left[ {}^{\mathcal{I} \rightarrow \mathcal{P}} \boldsymbol{\omega}_t \times \right] \quad (40)$$

where the cross-product matrix is

$$[\mathbf{v} \times] = \begin{bmatrix} 0 & -v_z & +v_y \\ +v_z & 0 & -v_x \\ -v_y & +v_x & 0 \end{bmatrix} \quad (41)$$

### 5.2 Measurement Update

Unit vectors sensed from star trackers, Earth or Sun sensors serve as the measurements in the MEKF. These measurements are provided to the MEKF as a pair of unit vectors in principal and inertial coordinates. The unit vectors in principal coordinates are sensed in the coordinates of the local sensor frame, and transformed into principal coordinates with knowledge of sensor mounting. The inertial unit vectors are calculated based on correspondences with an external reference (i.e. star catalog). The actual measurements,  $\mathbf{y}_t$ , and model measurements,  $\mathbf{h}_t$ , at time  $t$  are given by

$$\mathbf{y}_t = \begin{bmatrix} \mathbf{p}_1 \\ \mathbf{p}_2 \\ \vdots \\ \mathbf{p}_n \end{bmatrix}_t \quad (42)$$

$$\mathbf{h}_t = \begin{bmatrix} {}^{P \leftarrow I} \mathbf{R} \mathbf{i}_1 \\ {}^{P \leftarrow I} \mathbf{R} \mathbf{i}_2 \\ \vdots \\ {}^{P \leftarrow I} \mathbf{R} \mathbf{i}_n \end{bmatrix}_t + \begin{bmatrix} \nu_1 \\ \nu_2 \\ \vdots \\ \nu_n \end{bmatrix}_t \quad (43)$$

where  $\mathbf{R}$  is the direction cosine matrix corresponding to  $\mathbf{q}^{\mathcal{I} \rightarrow \mathcal{P}}$ ,  $\mathbf{i}$  and  $\mathbf{p}$  are unit vector observations expressed in the coordinates of  $\mathcal{I}$  and  $\mathcal{P}$ , respectively, and  $\boldsymbol{\nu}$  is zero-mean white Gaussian measurement noise.

The measurement sensitivity matrix,  $\mathbf{H} \in \mathbb{R}^{3n,3}$ , is given by

$$\mathbf{H}_t = \frac{\partial \mathbf{h}}{\partial \mathbf{x}} = [[\mathbf{h}_1 \times] \quad [\mathbf{h}_2 \times] \quad \dots \quad [\mathbf{h}_n \times]]^T \quad (44)$$

The measurement update is then

$$\mathbf{x}_{t+1|t+1} = \mathbf{x}_{t+1|t} + \mathbf{K}_t (\mathbf{y}_t - \mathbf{h}_t) \quad (45)$$

$$\boldsymbol{\Sigma}_{t+1|t+1} = \boldsymbol{\Sigma}_{t+1|t} - \mathbf{K}_t \mathbf{H}_t \boldsymbol{\Sigma}_{t+1|t} \quad (46)$$

where  $\mathbf{K}_t$  is the Kalman gain

$$\mathbf{K}_t = \boldsymbol{\Sigma}_{t|t-1} \mathbf{H}_t^T \left[ \mathbf{H}_t \boldsymbol{\Sigma}_{t|t-1} \mathbf{H}_t^T + \mathbf{R}_t \right]^{-1} \quad (47)$$

### 5.3 Attitude Update

After the measurement update, the relative attitude error encoded in  $\mathbf{x}_{t+1|t+1}$  can be used to correct the absolute attitude,  $\mathbf{q}^{\mathcal{I} \rightarrow \mathcal{P}}$ , as given by

$$\mathbf{q}_{t+1|t+1}^{\mathcal{I} \rightarrow \mathcal{P}} = \begin{bmatrix} 1 & +\alpha_z/2 & -\alpha_y/2 & +\alpha_x/2 \\ -\alpha_z/2 & 1 & +\alpha_x/2 & +\alpha_y/2 \\ +\alpha_y/2 & -\alpha_x/2 & 1 & +\alpha_z/2 \\ -\alpha_x/2 & -\alpha_y/2 & -\alpha_z/2 & 1 \end{bmatrix} \mathbf{q}_{t+1|t}^{\mathcal{I} \rightarrow \mathcal{P}} \quad (48)$$

After the absolute attitude is updated, the state vector is reset to zero. The attitude update does not modify the covariance, since it neither increases nor decreases uncertainty of the estimate; it merely transfers information internal to the MEKF.

## 6. HARDWARE-IN-THE-LOOP VERIFICATION

To verify the functionality and performance of the developed control and filtering architecture, a hardware-in-the-loop (HIL) testbed is created which stimulates the prototype telescope payload presented from Section 2 with a realistic stimulus as seen in Figure 6. This section will describe the interaction between these components.

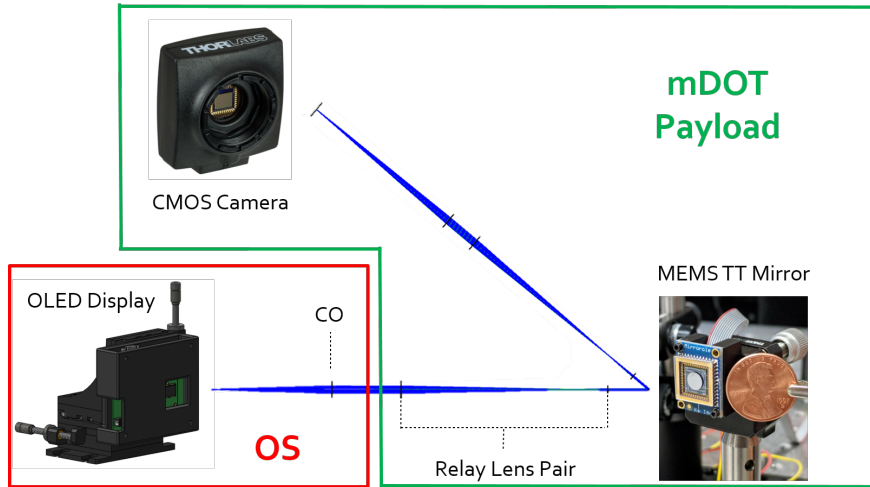


Figure 2. Hardware-in-the-loop architecture used to stimulate the telescope payload prototype.

## 6.1 OPTICAL STIMULATOR

An optical stimulator (OS) is used to stimulate the telescope payload with scenes highly representative of the space environment from a radiometric and geometric stand-point. The OS consists of an organic light emitting diode (OLED) monitor on a three-axis translational stage. The ground truth numerical simulation described in Section 3 is used to synthesize a scene composed of stellar and non-stellar objects which is then rendered to the monitor. The telescope payload prototype is stimulated by this scene through a corrective optic (CO), which corrects for the finite distance between the monitor and payload by collimating light emitted by the OLED, as seen in Figure 6.1.

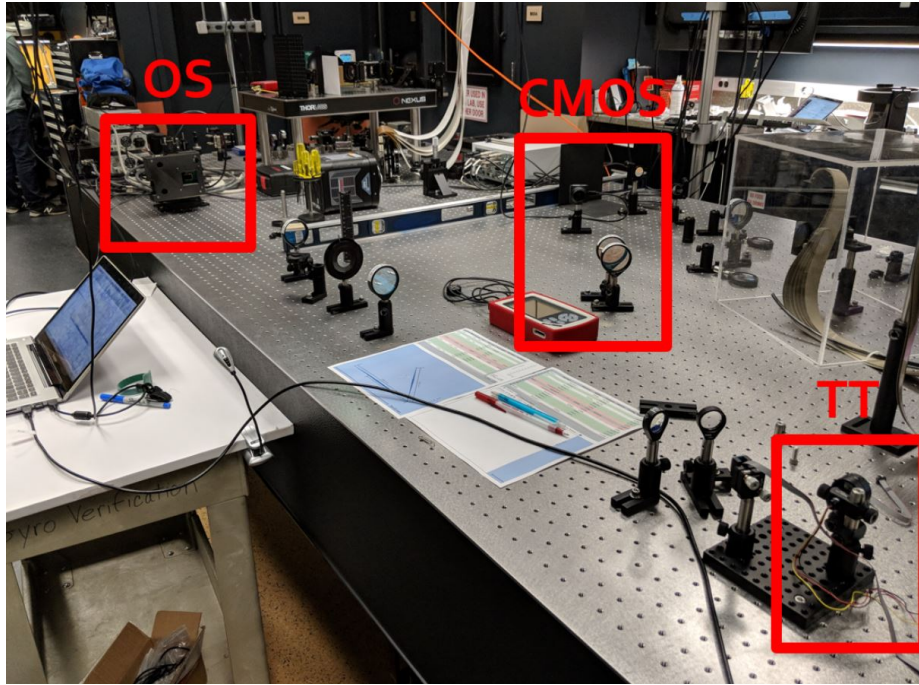


Figure 3. Hardware-in-the-loop testbed used to stimulate the telescope payload prototype. Light emitted from the OS is collimated by a CO before passing through the entrance pupil of the telescope payload prototype. A pair of lenses demagnifies the beam to fit on the 5 [mm] TT mirror. Additional optics are used to focus light reflected off the TT mirror onto the CMOS detector.

A ThorLabs S130C high-resolution optical power meter<sup>17</sup> was used to measure the radiometric flux passing through the pupil plane of the telescope payload. Irradiance measurements were gathered at different wavelengths and OS monitor digital count combinations. These measurements were used to identify the irradiance through the OS as a function of monitor state.<sup>18</sup> In addition to the radiometric calibration, a geometric calibration was performed to stimulate the telescope payload from a simulated angular origin in the presence of optical aberrations introduced by the CO. This is achieved by providing the rendering software with unit vector(s) which are a function of telescope payload stimulus unit vector(s) and the intrinsic parameters of the CO. The geometric calibration process<sup>18</sup> estimates the intrinsic parameters of the CO and dynamically warps the scene rendered to the monitor to offset the aberrations introduced by the CO.

The main limitation of this testbed is that OLED monitor refresh rate is 60 [Hz], which constrains the max temporal frequency that can be simulated in real time for a HIL experiment.

## 7. RESULTS

The simulation developed in Section 3 was used to drive the synthetic scene generation pipeline of the OS. Control actions computed by the telescope spacecraft GNC software are fed into the numerical simulation and are correspondingly reflected in the following OS scene rendering. Observations acquired by the telescope payload are then used in the MEKF measurement update. This sequence of events is connected in closed-loop and evolves dynamically.

Initially the vehicle is not pointing in the desired orientation by large angular offset in all axes. This triggers the path planner to compute a slew maneuver about the eigenaxis connecting the initial and desired frames. As seen in Figure 7, the total rotation angle,  $E_\theta$ , about this axis is initially large, however the reaction wheel control loop instead tracks a smaller magnitude moving reference signal,  $e_\theta$ , which temporally evolves based on Equation 35. The relative attitude to this moving reference defined by an eigenaxis and local rotation angle are used to construct the error quaternion fed into the non-linear control law in Equation 29.

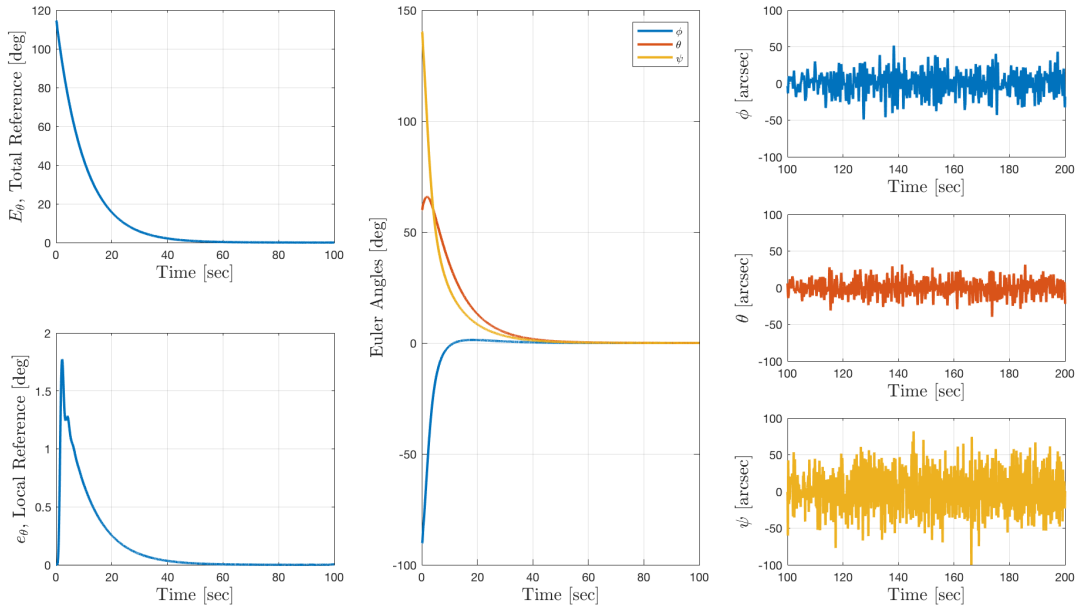


Figure 4. Path planning used for coarse attitude control slews about the Eigen-axis between the initial and desired frames. The total angular error about the slew axis,  $E_\theta$  decays through the utilization of a smaller moving reference angle,  $e_\theta$ . The error Euler angles in the center plot between the initial and desired frame decay to coarse pointing accuracy of the BCT XACT unit defined in Table 1.

Once coarse pointing has been achieved to within 1 [deg], the telescope payload will be able to identify and centroid the LED reference beacon on the occulter spacecraft. Residual pointing jitter will result in the occulter reference beacon sweeping over multiple pixels as its angular position relative to the telescope payload evolves in time. This motion is reflected in closed-loop by continuously updating the synthesized scene rendered to the OS monitor. With a detected reference beacon, the TT control loop is closed after coarse pointing is achieved to within 0.1 [deg]. As outlined in the control architecture section, bearing angles to the reference beacon are used to compute differential updates to the angular position of the TT mirror. The impact of the TT loop closure is depicted in Figure 5, which results in the pixel plane trace of the reference beacon being stabilized to within 300 [mas] at  $3\sigma$ .

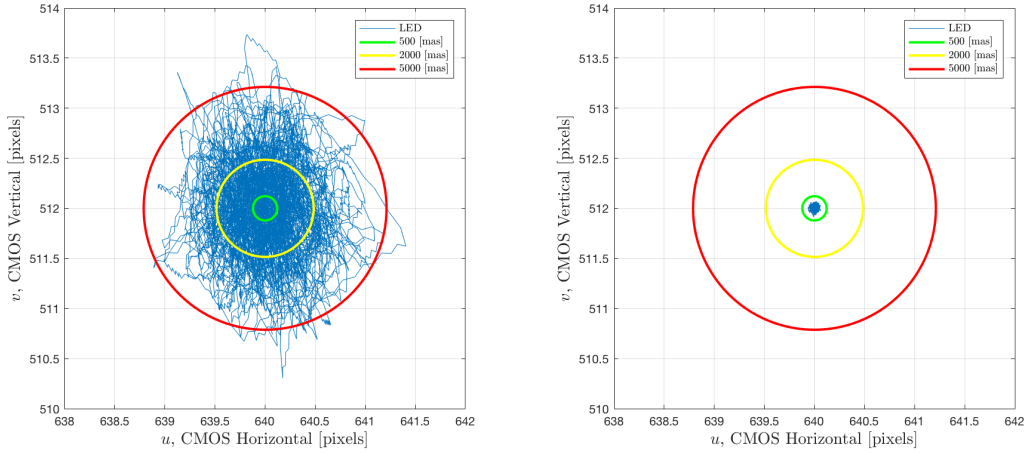


Figure 5. Simulated traces of the occulter reference LED motion on the telescope CMOS detector. Left: coarse pointing control using reaction wheels and no TT results in approximately 10 [as] level consistent with that of the BCT XACT unit. Right: TT loop is closed and the LED motion on the CMOS detector is stabilized to within 300 [mas] at  $3\sigma$ . Contours are overlaid on plots to depict achieved angular precision.

The nominal reaction wheel speed in Figure 5 is 3500 [rpm], which contains a predominant disturbance harmonic at 60 [Hz] based off the BCT15 reaction wheel data described in Section 3.3.5. This 60 [Hz] mode is well within the frequency at which the TT mirror can temporally respond to, however internal reaction wheel disturbance harmonics vary in frequency as a function of wheel speed. For example, at reaction wheel speeds of 2500 [rpm], the predominant disturbance harmonic is at 330 [Hz], as shown in the left-hand side of Figure 6. These higher frequency disturbances closer to the bandwidth of the TT mirror are more difficult to reject. This phenomenon can be observed in the degraded image stabilization depicted in the right-hand side of Figure 6.

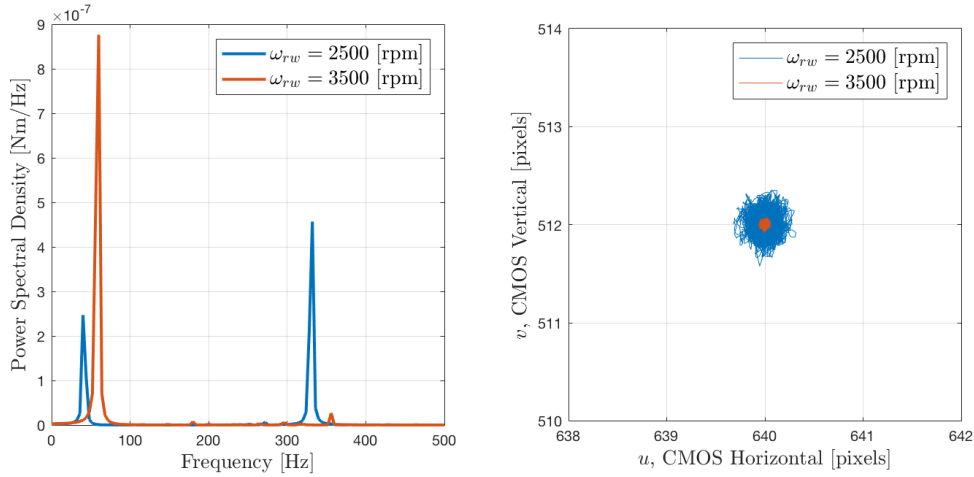


Figure 6. Left: power spectral density of the reaction wheel disturbances at different nominal wheel speeds. Right: motion of the occulter LED beacon on the CMOS detector based on two simulations with reaction wheel speeds of 2500 and 3500 [rpm].

Figure 6 shows that momentum and reaction wheel speed management will be necessary to avoid encountering unfavorable disturbance harmonics during the mDOT science observation phase.

## 8. CONCLUSION

This paper develops a two stage attitude control architecture for achieving high precision pointing necessary to directly image exoplanets with a CubeSat telescope. Coarse pointing with reaction wheels is achieved through a non-linear control law which cancels out gyroscopic coupling and utilizes proportional-derivative control to orient the vehicle and track a desired angular velocity. A path planner is presented which slews the vehicle along the eigenaxis between the initial and desired attitude. Tracking performance is increased by utilizing higher gains in conjunction with a reference signal being updated smoothly with a first order differential equation.

Since the pointing precision of reaction wheels is limited to tens of arcseconds, an image stabilization control loop is utilized to stabilize motion of the dim target exoplanet on the CMOS sensor for long integration exposures. This image stabilization loop consists of a TT mirror steering bright light from an LED beacon on the occulter spacecraft to a reference location on the telescope CMOS sensor. Bearing angles to this beacon are computed and used to apply differential corrections to the angular position of the TT mirror.

A detailed simulation was created to verify the functionality and performance of this control architecture. This simulation was then utilized as the ground truth for a HIL test using the OS as a stimulus, and a payload prototype as the sensor. The OS consists of an OLED monitor stimulating the telescope payload through a CO. The numerically simulated evolution of the vehicle's attitude is used to render a geometrically and radiometrically consistent star field and occulter LED beacon to the OS monitor.

Although precision pointing at the sub-arcsecond level was achieved in this study, further work must be done to package this prototype into a CubeSat scale payload. Additionally, a momentum management strategy needs to be formulated to ensure that unfavorable reaction wheel harmonics are avoided during the duration of the science observation phase.

## ACKNOWLEDGMENTS

The authors are grateful to Adam Koenig, Michael Taylor, and Ewan Douglas for their helpful discussions. The authors would also like to thank Joel Shields for making experimental reaction wheel data available for use in this study. This work was supported in part by U.S. Air Force Research Laboratory's Control, Navigation, and Guidance for Autonomous Spacecraft (CoNGAS) contract FA9453-16-C-0029.

## REFERENCES

- [1] Borucki, W. J., Koch, D. G., Lissauer, J. J., Basri, G. B., Caldwell, J. F., Cochran, W. D., Dunham, E. W., Geary, J. C., Latham, D. W., Gilliland, R. L., et al., "The kepler mission: a wide-field-of-view photometer designed to determine the frequency of earth-size planets around solar-like stars," in [*Future EUV/UV and Visible Space Astrophysics Missions and Instrumentation*], **4854**, 129–141, International Society for Optics and Photonics (2003).
- [2] Cash, W., "Detection of earth-like planets around nearby stars using a petal-shaped occulter," *Nature* **442**(7098), 51 (2006).
- [3] Kolmas, J., Banazadeh, P., Koenig, A., Macintosh, B., and D'Amico, S., "System design of a miniaturized distributed occulter/telescope for direct imaging of star vicinity," in [*IEEE Aerospace Conference Proceedings*], Loew, M. H., ed., 1–11 (2016).
- [4] Koenig, A. W., D'Amico, S., Macintosh, B., and Titus, C. J., "Formation design analysis for a miniaturized distributed occulter/telescope in earth orbit," in [*International Symposium on Space Flight Dynamics (ISSFD)*], DLR's German Space Operations Center (GSOC) and ESA's European Space Operations Center Munich (2015).
- [5] Koenig, A. W., D'Amico, S., Macintosh, B., and Titus, C. J., "A pareto-optimal characterization of miniaturized distributed occulter/telescope systems," in [*Techniques and Instrumentation for Detection of Exoplanets VII*], **9605**, International Society for Optics and Photonics (2015).
- [6] Koenig, A. W., D'Amico, S., Macintosh, B., and Titus, C. J., "Optimal formation design of a miniaturized distributed occulter/telescope in earth orbit," in [*Proceedings of the AIAA/AAS Astrodynamics Specialist Conference*], (2015).

- [7] Board, S. S. et al., “Panel reports—new worlds, new horizons in astronomy and astrophysics,” (2011).
- [8] Knapp, M., Seager, S., Smith, M., and Pong, C., “Asteria: Arcsecond space telescope enabling research in astrophysics,” in [*AGU Fall Meeting Abstracts*], (2017).
- [9] Blue Canyon Technologies, *BCT XACT High Performance Attitude Control for CubeSats Datasheet* (2018).
- [10] Mirrorcle Technologies, *Gimbal-Less Two-Axis Scanning MEMS Micromirrors. Device Datasheet S6180* (2018).
- [11] ThorLabs, *1/2-Inch Megapixel CMOS Digital Image Sensor MT9M001C12STM* (2004).
- [12] Giraldo, V. and D’Amico, S., [*Development of the Stanford GNSS Navigation Testbed for Distributed Space Systems*], Institute of Navigation, International Technical Meeting, Reston, Virginia (2018).
- [13] Wertz, J. R., [*Spacecraft Attitude Determination and Control*], vol. 73, Springer Science & Business Media (2012).
- [14] Shields, J., Pong, C., Lo, K., Jones, L., Mohan, S., Marom, C., McKinley, I., Wilson, W., and Andrade, L., “Characterization of cubesat reaction wheel assemblies,” *Journal of Small Satellites* **6**(1), 565–580 (2017).
- [15] Lefferts, E. J., Markley, F. L., and Shuster, M. D., “Kalman filtering for spacecraft attitude estimation,” *Journal of Guidance, Control, and Dynamics* **5**(5), 417–429 (1982).
- [16] Markley, F. L., “Attitude error representations for kalman filtering,” *Journal of guidance, control, and dynamics* **26**(2), 311–317 (2003).
- [17] Micron, *S130C - Slim Photodiode Power Sensor Datasheet* (2018).
- [18] Beierle, C., Sullivan, J., and D’Amico, S., “High-fidelity verification of vision-based sensors for inertial and far-range spaceborne navigation,” in [*26th International Symposium on Space Flight Dynamics (ISSFD), Matsuyama, Japan*], (2017).